JℱM PAPERS

A class of instabilities induced by surface vibrations

N.N. Haq[1] and **J.M. Floryan**[1]

[1]Department of Mechanical and Materials Engineering, The University of Western Ontario, London, ON N6A 5B9, Canada
Corresponding author: J.M. Floryan, floryan@uwo.ca

We consider the stability of Couette flow when travelling vibrations perturb one boundary. It is demonstrated that if the bounding surface profile takes the form of sinusoidal waves, then the otherwise stable shear flow becomes unstable for appropriately chosen values of vibration amplitude, phase speed and wavenumber. When instability arises, it is driven by centrifugal forces that are created by wave-imposed changes in the direction of fluid movement. Only subcritical waves, defined as vibrations with phase speed smaller than the maximum flow velocity, cause instability. As the fluid Reynolds number grows, the interval of vibration wavenumbers and phase speeds capable of flow destabilisation is enhanced. A range of parameters is identified for which the vibrations seem to play dual roles: they decrease the flow resistance while simultaneously generating streamwise vortices. This vibration class constitutes an energy-efficient control tool that may potentially intensify the mixing within a flow.

Key words: drag reduction, mixing enhancement

1. Introduction

Vibrations can play a pivotal role in determining the properties of a wide range of fluid motions. Sometimes, in mechanical systems, vibrations are both unavoidable and undesirable because they may make the flow sensitive to instability and prone to premature breakdown to turbulence. On the other hand, vibrations can be used quite intentionally as a flow control method to reduce the flow resistance or to provide a propulsive effect. In other applications, we wish to actively encourage the vibrations of the conduit to enhance fluid mixing, including inducing low Reynolds number chaos (Gepner & Floryan 2020). Then, of course, one is interested in determining changes in the fundamental

flow properties caused by vibrations. Furthermore, vibrations are known to play a role in various environmental flow phenomena, with the classic example prototype example provided by Langmuir circulation, which is driven by wind that blows waves across the surface of an expanse of water (Leibovich 1983; Thorpe 2004).

Our concern in this work is to provide insight into the stability of shear flows affected by vibrations used as an active control tool. The principal goal of this class of problems is to devise a strategy such that energy saving from drag reduction exceeds the energy expended in applying the control. Until recently, it was thought that this goal was unachievable (Bewley 2009), but this view has been challenged recently (Floryan 2023). In the work described below, we consider an active flow distributed propulsion system in which part of the externally supplied energy is used to reduce the resistance rather than overcome it. However, rather than just measuring the effectiveness of the process in terms of an energy balance assuming no change in the performance of the system, we attempt to improve matters by enhancing the propulsion energy (Haq & Floryan 2022; Floryan, Aman & Panday 2023b). The concept of distributed propulsion is not new and has a long history within various biological flows (Taylor 1951; Blake & Sleigh 1974; Katz 1974; Brennen & Winet 1977; Chan, Balmforth & Hosoi 2005; Lee *et al.* 2008; Lauga 2016). More recently, other instances of distributed propulsion have been investigated at larger scales; some examples include nonlinear streaming created by wall transpiration (Jiao & Floryan 2021), the so-called pattern interaction effect (Floryan & Inasawa 2021) that leads to thermal drift (Abtahi & Floryan 2017), patterned heating (Floryan & Floryan 2015), nonlinear thermal streaming (Floryan *et al.* 2023), thermal waves (Hossain & Floryan 2023) and wall vibrations (Floryan & Haq 2022). The previously mentioned biological examples of distributed propulsion occur on such short scales that the stability of the flow is ensured, but this issue is not so clear-cut when dealing with the other problems. To date, scant attention has been paid to this question, and it is this problem that we seek to address herein.

We tackle our task by selecting a straightforward paradigm problem free from as many superfluous and distracting effects as is feasible. To that end, we focus on the instabilities caused by vibrations in wall-bounded shear layers. More precisely, we investigate the effect of wall vibrations on two-dimensional laminar Couette flow. Since this flow is linearly stable without vibrations (Romanov 1972), we can be assured that any instability can be ascribed to the imposition of vibration rather than being an intrinsic property of the motion. It is already known that this flow can be destabilised using modifications produced by wall transpiration (Jiao & Floryan 2021) and surface grooves (Floryan 2002), but its response to wall vibrations is unknown. We focus on disturbances that form streamwise vortices and explore the system response across a wide range of vibration wavelengths and phase speeds. Our calculations are restricted to cases in which the amplitude of the vibrations is less than about 5 % of the slot opening. There are two reasons for this. First, any uncontrolled vibrations generally are of small amplitude, as any system susceptible to larger unwanted vibrations normally necessitates a complete redesign. Conversely, when the vibrations are intentional, they are frequently created using piezoelectric actuators characterised by small-amplitude and high-frequency displacements. Finally, we mention limiting the flow Reynolds number to less than 2000 as we are interested in laminar flows. Experimental evidence suggests that Couette flow becomes turbulent at larger Reynolds numbers (Tillmark & Alfredsson 1992).

Our control strategy belongs to a class of problems that uses a spatial pattern of actuation rather than relying solely on the strength of the forcing. In most circumstances, it is thought that using a pattern-based control is typically associated with lower energy actuation costs. One question in pattern-based control is how best to select the spatial distribution. Clearly,
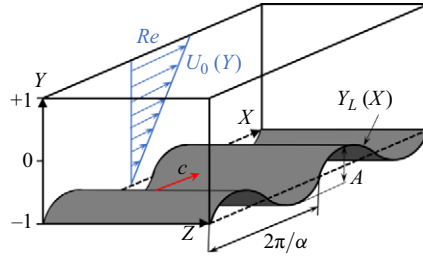
Figure 1. Schematic diagram of the flow system.

an almost limitless range of options is available, and exploring them on a case-by-case basis is not feasible. If the pattern is spatially periodic, then it is natural to write the profile of the wall vibration using an appropriate Fourier series. In our analysis, we will suppose that the wall shape is just a single Fourier mode of a given wavelength. While this may seem somewhat over-simplistic, there is evidence that the flow characteristics over a wall of a more general profile can be well modelled by the single component if chosen carefully (Floryan 2007). The reduced model identifies those parts of Fourier space that are hydraulically active by considering the projection of an arbitrary pattern onto Fourier space and determining whether any dynamically important components are involved.

To understand how wall vibrations can influence the stability of wall-bounded shear flows, we organise the remainder of the paper in the following way. In § 2, we describe our idealised two-dimensional model problem that consists of an infinite slot bounded by a translating smooth upper plate and a lower surface whose shape takes the form of travelling waves. Then, in § 3, we isolate the primary state of the flow, i.e. the Couette flow modified by the vibrations. This basic state requires a numerical solution of the relevant field equations. Once this has been found, we move on to § 4, which outlines the key stability problem and discusses the numerical solution of the disturbance equations. Most of our results are collected in § 5, where the characteristics of flow instabilities caused by wall vibrations are described. The paper closes with a few final remarks and observations.

2. Problem formulation

Consider flow in a slot driven by movement of the upper plate with a prescribed velocity U_{top} while the lower plate is stationary. The slot extends to $\pm\infty$ in the X- and Z-directions with plates placed at a distance $2h$ apart, as shown in figure 1. The lower plate is exposed to vibrations in the form of a sinusoidal travelling wave, resulting in the time-dependent slot geometry of the form

$$Y_L(t, X) = -1 + \tfrac{1}{2}\cos[\alpha\,(X - ct)], \tag{2.1}$$

where subscript L refers to the lower plate, and h was used as the length scale.

The velocity vector $V = (u, v, w)$ is scaled with the viscous velocity scale $U_v = v/h$, the pressure p is scaled with ρU_v^2 (where ρ denotes the fluid density), and the time t is scaled with h/U_v. The relevant boundary conditions are

for $Y = 1$, $\quad u = Re,\ v = 0,\ w = 0,\qquad$ for $Y = Y_L(t, X)$, $\quad u = 0,\ v = \dfrac{\partial Y_L}{\partial t},\ w = 0,$

$$\tag{2.2a–f}$$

where

$$Re \equiv U_{top}h/v \tag{2.3}$$

is the Reynolds number. Since the flow is driven solely by the movement of the upper plate, the pressure gradient constraint in the form

$$\frac{\partial p}{\partial X}\bigg|_m = 0, \tag{2.4}$$

where subscript m denotes the mean value, must be imposed.

It is simpler to carry out detailed calculations using the frame of reference moving with the wave, which leads to Galileo's transformation of the form

$$x = X - ct, \quad y = Y, \quad z = Z. \tag{2.5a–c}$$

The complete problem formulation can now be written as

$$\frac{\partial u}{\partial t} + (u - c)\frac{\partial u}{\partial x} + v\frac{\partial u}{\partial y} + w\frac{\partial u}{\partial z} = -\frac{\partial p}{\partial x} + \frac{\partial^2 u}{\partial x^2} + \frac{\partial^2 u}{\partial y^2} + \frac{\partial^2 u}{\partial z^2}, \tag{2.6a}$$

$$\frac{\partial v}{\partial t} + (u - c)\frac{\partial v}{\partial x} + v\frac{\partial v}{\partial y} + w\frac{\partial v}{\partial z} = -\frac{\partial p}{\partial y} + \frac{\partial^2 v}{\partial x^2} + \frac{\partial^2 v}{\partial y^2} + \frac{\partial^2 v}{\partial z^2}, \tag{2.6b}$$

$$\frac{\partial w}{\partial t} + (u - c)\frac{\partial w}{\partial x} + v\frac{\partial w}{\partial y} + w\frac{\partial w}{\partial z} = -\frac{\partial p}{\partial z} + \frac{\partial^2 w}{\partial x^2} + \frac{\partial^2 w}{\partial y^2} + \frac{\partial^2 w}{\partial z^2}, \tag{2.6c}$$

$$\frac{\partial u}{\partial x} + \frac{\partial v}{\partial y} + \frac{\partial w}{\partial z} = 0, \tag{2.6d}$$

$$\text{for } y = 1, \quad u = Re, \ v = 0, \ w = 0, \tag{2.6e–g}$$

$$\text{for } y = y_L(x) = -1 + \frac{1}{2}\cos[\alpha(X - ct)], \quad u = 0, \ v = -c\frac{\mathrm{d}y_L(x)}{\mathrm{d}x}, \ w = 0, \tag{2.6h–j}$$

$$\frac{\partial p}{\partial x}\bigg|_{mean} = 0. \tag{2.6k}$$

The next section begins with a detailed analysis of the two-dimensional stationary state in the moving reference frame.

3. Determination of the primary state

The primary state has the form of a two-dimensional stationary flow in the moving frame of reference, i.e. $w = 0$, $\partial/\partial z = 0$, $\partial/\partial t = 0$. This flow is expected to bifurcate to a secondary state consisting of streamwise vortices. This analysis aims to determine critical conditions leading to such a bifurcation. We begin with a discussion of the properties of the stationary state before proceeding to stability analysis.

3.1. *Problem formulation and numerical solution*

The translation of the upper plate in the absence of any vibrations creates a simple Couette flow. The velocity field $\boldsymbol{v_0}$, pressure p_0, pulling force applied to the upper plate (per unit length and width) F_0, shear acting on the upper plate τ_0, and flow rate Q_0 are given by

$$\boldsymbol{v}_0(x, y) = [u_0, v_0] = \left[\tfrac{1}{2}(1 + y), 0\right], \quad p_0(x, y) = \text{constant}, \quad F_0 = \tfrac{1}{2}, \quad \tau_0 = -\tfrac{1}{2}, \quad Q_0 = 1.$$
$$(3.1a\text{--}e)$$

Here, the velocity of the upper plate U_{top} has been adopted as the velocity scale, ρU_{top}^2 as the pressure scale, and $U_{top}\mu/h$ as the surface force scale, and the flow rate was scaled using U_{top}. To describe the effects of surface vibrations, we represent the total flow quantities as a sum of the reference flow and the vibration-induced modifications, i.e.

$$\boldsymbol{V}(x, y) = [u_B(x, y), v_B(x, y)] = [Re\, u_0(y) + u_{1,B}(x, y), v_{1,B}(x, y)], \quad (3.2a)$$

$$p_B(x, y) = C + p_{1,B}(x, y), \quad \psi_B(x, y) = Re\, \psi_0(y) + \psi_{1,B}(x, y), \quad (3.2b,c)$$

$$Q_{B,mean} = Re + Q_{1B,mean}, \quad \tau_B(x) = -\tfrac{1}{2}Re + \tau_{1,B}(x), \quad F_B = \tfrac{1}{2}Re + F_{1,B}.$$
$$(3.2d\text{--}f)$$

In the above, (u_B, v_B), p_B, ψ_B, $Q_{B,mean}$, τ_B and F_B denote the complete velocity, pressure, stream function, mean flow rate, shear, and pulling force, respectively, and $(u_{1,B}, v_{1,B})$, $\psi_{1,B}$, $p_{1,B}$, $Q_{1B,mean}$ and $F_{1,B}$ denote the velocity, stream function, pressure, mean flow rate, and pulling force modifications caused by vibrations. We eliminate pressure by introducing stream function modifications $\psi_{1,B}$ defined as

$$u_{1,B} = \frac{\partial \psi_{1,B}}{\partial y}, \quad v_{1,B} = -\frac{\partial \psi_{1,B}}{\partial x}. \quad (3.3a,b)$$

Taking the y-derivative of (3.2a) and the x-derivative of (3.2b), and subtracting the latter from the former, leads to the formulation of the form

$$\boldsymbol{\nabla}^2\left(\boldsymbol{\nabla}^2 \psi_{1,B}\right) - (Re\, u_o - c)\frac{\partial}{\partial x}\boldsymbol{\nabla}^2 \psi_{1,B} + Re\,\frac{\mathrm{d}^2 u_o}{\mathrm{d}y^2}\frac{\partial \psi_{1,B}}{\partial x} = N_{uv}, \quad (3.4)$$

$$\text{for } y = +1, \quad \frac{\partial \psi_{1,B}}{\partial y} = 0, \quad \frac{\partial \psi_{1,B}}{\partial x} = 0, \quad (3.5a,b)$$

$$\text{for } y = y_L(x), \quad \frac{\partial \psi_{1,B}}{\partial y} = -Re\, u_0, \quad \frac{\partial \psi_{1,B}}{\partial x} = c\,\frac{\mathrm{d}y_L}{\mathrm{d}x}. \quad (3.5c,d)$$

In the above, $N_{uv} \equiv (\partial/\partial y)((\partial/\partial x)(\widehat{u_{1,B}u_{1,B}}) + (\partial/\partial y)(\widehat{u_{1,B}v_{1,B}})) - (\partial/\partial x)((\partial/\partial x)$ $(\widehat{u_{1,B}v_{1,B}}) + (\partial/\partial y)(\widehat{v_{1,B}v_{1,B}}))$, and hats denote products of quantities. The above system needs to be supplemented by the pressure gradient constraint (2.6k), whose explicit form depends on the type of discretisation.

The discretisation process begins with the transformation

$$\hat{y} = 2\,\frac{y - 1}{y_b + 2} + 1, \quad \Gamma = \frac{\mathrm{d}\hat{y}}{\mathrm{d}y}, \quad (3.6)$$

which maps the strip $y \in (-1 - y_b, 1)$ in the y-direction into the strip $\hat{y} \in (-1, 1)$ in the $\hat{y}$-direction. Here, y_b denotes the location of the lower extremity of the lower plate. This preliminary step is required to use the standard definition of Chebyshev polynomials in discretisation. The unknowns are expressed in terms of Fourier expansions of the form

$$q(x, \hat{y}) = \sum_{n=-N_B}^{+N_B} q^{(n)}(\hat{y})\, \mathrm{e}^{in\alpha x}, \quad (3.7)$$

where q stands for any of the following quantities: $\psi_{1,B}, u_{1,B}, v_{1,B}, \widehat{u_{1,B}u_{1,B}}$, $\widehat{u_{1,B}v_{1,B}}, \widehat{v_{1,B}v_{1,B}}$, and the modal functions $q^{(m)}(\hat{y})$ satisfy the reality conditions, i.e. $q^{(m)}$ is the complex conjugate of $q^{(-m)}$. Substitution of (3.7) into (3.4), and separation of Fourier modes, lead to a system of nonlinear ordinary differential equations of the form

$$
\begin{aligned}
\Big[&-2n^2\alpha^2\Gamma^2 D^2 + \Gamma^4 D^4 + (n\alpha)^4 - in\alpha(Re\,u_o - c)(\Gamma^2 D^2 - (n\alpha)^2) \\
&+ in\alpha\,Re\,\Gamma^2 D^2 u_0 \Big]\,\psi_{1,B}^{(n)}(y) = in\alpha\Gamma D\,\widehat{u_{1,B}u_{1,B}}^{(n)} + (\Gamma^2 D^2 + (n\alpha)^2)\,\widehat{u_{1,B}v_{1,B}}^{(n)} \\
&- in\alpha\Gamma D\,\widehat{v_{1,B}v_{1,B}}^{(n)},
\end{aligned}
\tag{3.8}
$$

where $D = d/d\hat{y}$, and the right-hand side provides coupling between different modes. These equations need to be supplemented by the relevant form of boundary conditions. Boundary conditions at the upper plate can be set explicitly for each Fourier mode, i.e.

$$
\text{for } y = 1, \quad \psi_{1,B}^{(n)} = 0 \text{ for } n \neq 0, \quad \Gamma D\psi_{1,B}^{(n)} = 0. \tag{3.9a,b}
$$

Since (3.9a) does not include mode zero, the relevant boundary conditions required separate development described below. Boundary conditions at the lower plate involve a combination of modes coupled through the plate geometry. We start by expressing them in terms of the stream function in the form

$$
\text{for } y = y_L(x), \quad \psi_{1,B} = \frac{c}{\Gamma}\frac{d\widehat{y_L}}{dx}, \quad \Gamma D\psi_{1,B} = -Re\,u_0. \tag{3.10a,b}
$$

The condition (3.5d) is written in an alternative way by noting that variations in ψ_B along the lower plate can be expressed as

$$
\psi_B = Re\,\psi_0 + \psi_{1,B} = \left(\frac{\partial\psi_B}{\partial x}\,dx + \frac{\partial\psi_B}{\partial\hat{y}}\,d\hat{y}\right)\Bigg|_{\hat{y}_L(x)} = \frac{c}{\Gamma}\frac{d\hat{y}_L}{dx}\,dx. \tag{3.11}
$$

Integrating (3.11) along this plate yields

$$
\psi_{1,B}(x) = \frac{c}{\Gamma}\left[\hat{y}_L(x) - \hat{y}_L(x_0)\right] - Re\,\psi_0(\hat{y}_L), \tag{3.12}
$$

where the constant of integration was selected by assuming that $\psi_{1,B}(x_0) = 0$, with x_0 being an arbitrary point along the plate. The stream function is constant along the upper plate, i.e. $\psi_B = G$, where G needs to be determined from the pressure gradient constraint. This constraint can be expressed as

$$
D^2\psi_{1,B}^{(0)}(1) - D^2\psi_{1,B}^{(0)}(-1) = \Gamma^{-2}\left[\widehat{u_1v_1}^{(0)}(1) - \widehat{u_1v_1}^{(0)}(-1)\right], \tag{3.13}
$$

with details of the derivation explained in Appendix A. The reader may note that this constraint involves both ends of the solution domain. Expressing the remaining conditions using modal functions requires invoking the immersed boundary conditions method.

The ordinary differential equations (3.8) arising from Fourier decomposition were discretised by expressing modal functions as Chebyshev expansions, and algebraic equations for the expansion coefficients were constructed using the Galerkin projection method. The irregularity of the flow domain was handled using the spectrally accurate immersed boundary conditions method, with flow boundary conditions replaced by constraints. Details of implementations of these conditions are omitted from this presentation due to their excessive length, but can be found in Szumbarski & Floryan (1999) and Husain, Szumbarski & Floryan (2009). These constraints were implemented using the tau method (Canuto *et al.* 1992). The overall algorithm is gridless and spectrally

accurate. The computations were carried out with at least five-digit accuracy, and this requirement was satisfied by selecting the required number of Fourier modes and Chebyshev polynomials to be used in the computations.

In the solution process, the right-hand side of (3.8) was assumed to be known (taken from the previous iteration), and the system was solved to provide a new approximation for $\psi_{1,B}(x, \hat{y})$. A new approximation for velocity components was determined, leading to a new approximation of the right-hand side, then a new approximation for $\psi_{1,B}(x, \hat{y})$ was computed. The process was continued until convergence was achieved.

The stability analysis requires knowledge of the velocity vector $\boldsymbol{V}_B = (u_B, v_B, 0)$ and the vorticity vector $\boldsymbol{\omega}_B = (\xi_B, \eta_B, \phi_B) = (0, 0, \partial v_B/\partial x - \partial u_B/\partial y)$ of the stationary state. These quantities were determined in the post-processing stage and were represented as

$$\left[u_B, v_B, \phi_B \right](x, \hat{y}) = \sum_{n=-N_B}^{N_B} \left[f_u^{<n>}, f_v^{<n>}, f_\phi^{<n>} \right](\hat{y}) \; \mathrm{e}^{\mathrm{i}n\alpha x}. \tag{3.14}$$

3.2. *Properties of the primary state*

Vibrations propel the fluid along the lower plate using the peristaltic effect, thus reducing the relative fluid velocity with respect to the moving plate and reducing shear stress at that plate. Reduction of flow resistance was discussed extensively in Floryan & Haq (2022). Its effectiveness can be gauged by determining the external force required to maintain the movement of the upper plate at the same velocity with and without vibrations. The shear stress on the upper plate was integrated over a wavelength to determine the vibrations-induced change of the pulling force. The shear stress $\sigma_{Xv,U}$ that acts on the fluid and the external pulling force (per unit length and width) on the upper plate F_B are given by

$$\sigma_{xv,U} = \left. \frac{\partial u_B}{\partial y} \right|_{y=1}, \quad F_B = \lambda^{-1} \int_0^\lambda \left. \frac{\partial u_B}{\partial y} \right|_{y=1} \mathrm{d}x, \tag{3.15a,b}$$

where $\lambda = 2\pi/\alpha$ denotes wavelength. The force correction can be evaluated as

$$F_{1,B} = F_B - \tfrac{1}{2}Re, \tag{3.15c}$$

and its negative values correspond to a reduction of the required external force.

Figure 2 illustrates variations of $F_{1,B}$ normalised as $F_{norm} = (F_{1,B})/(Re \, F_0 A^2)$. The resistance reduction zones are greyed for easy identification. The c-axis can be divided into two zones. The lower zone corresponds to $0 < c < Re$, i.e. the wave velocity is in the fluid velocity range. Such waves are called subcritical (Floryan & Haq 2022). The upper zone corresponds to $c > Re$, i.e. these waves are faster than the fluid and are called supercritical. The supercritical waves generally reduce flow losses, with this reduction changing in a fairly regular manner and increasing with c and α. The subcritical waves exhibit complex behaviour that changes with Re – they generally increase flow losses, but there are islands in the parameter space where they decrease losses, so making generalisations is difficult. The natural flow frequencies of the Orr–Sommerfeld modes in the absence of vibrations overlap with the subcritical waves, but no near resonance was observed.

An analysis of the flow modifications provides another view of the flow response. Figure 3 shows how subcritical waves modify the streamwise component profiles. These structures are concentrated in the boundary layer adjacent to the vibrating wall when the waves are sufficiently short, as illustrated in the third column in figure 3. The fluid outside the boundary layer behaves as if this layer were a wall moving with the velocity correction outside the boundary layer having the form of Couette flow driven by the velocity at the edge of the boundary layer. This type of response has previously been
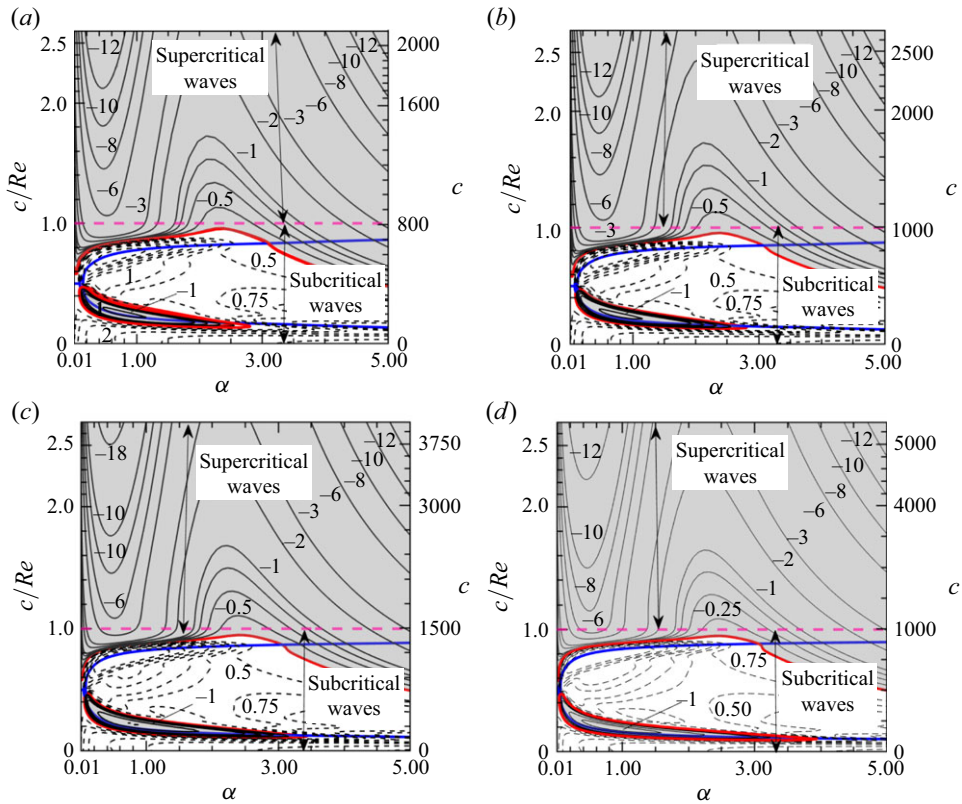
Figure 2. Variations in the normalised force correction $F_{norm} = F_{1,B}/(Re\, F_0 A^2)$ as a function of α and c for (a) $Re = 800$, (b) $Re = 1000$, (c) $Re = 1500$, (d) $Re = 2000$. The grey shading indicates negative values; the red line shows conditions giving $F_{1,B} = 0$; zones between the blue lines provide the range of natural frequencies of the Orr–Sommerfeld modes in the absence of vibrations.

referred to as a 'moving wall' pattern (Floryan & Haq 2022). By contrast, long waves seem to produce modifications in the form of a sloshing-type behaviour that extends across the whole slot, with the forward movement occurring around the wave troughs, and the backward movement near the crests. Unsurprisingly, modes of an intermediate wavelength are somewhat of a hybrid of these two extremes: the middle column of figure 3 shows some structure concentration near the vibrating wall, while some sloshing still penetrates the slot interior. The character of the flow response remains qualitatively the same regardless of the flow Reynolds number (details not shown).

4. Formulation of the linear stability theory and its numerical solution

We have now seen how the imposed wall vibrations modify the basic state, and this raises the possibility that this new state may possess stability characteristics qualitatively very different from the unmodified (linearly stable) Couette flow (Romanov 1972). We investigate this question here, focusing on possible instabilities leading to streamwise vortices forming.

We begin by writing the governing equations in the moving frame of reference expressed in terms of the vorticity transport and continuity equations, i.e.

$$\frac{\partial \boldsymbol{\omega}}{\partial t} - (\boldsymbol{\omega}.\boldsymbol{\nabla})\,\boldsymbol{V} + (\boldsymbol{V}.\boldsymbol{\nabla})\,\boldsymbol{\omega} - c\frac{\partial \boldsymbol{w}}{\partial x} = \boldsymbol{\nabla}^2 \boldsymbol{\omega}, \quad \boldsymbol{\nabla}.\boldsymbol{V} = 0, \quad \boldsymbol{\omega} = \boldsymbol{\nabla} \times \boldsymbol{V}. \qquad (4.1a\text{–}c)$$
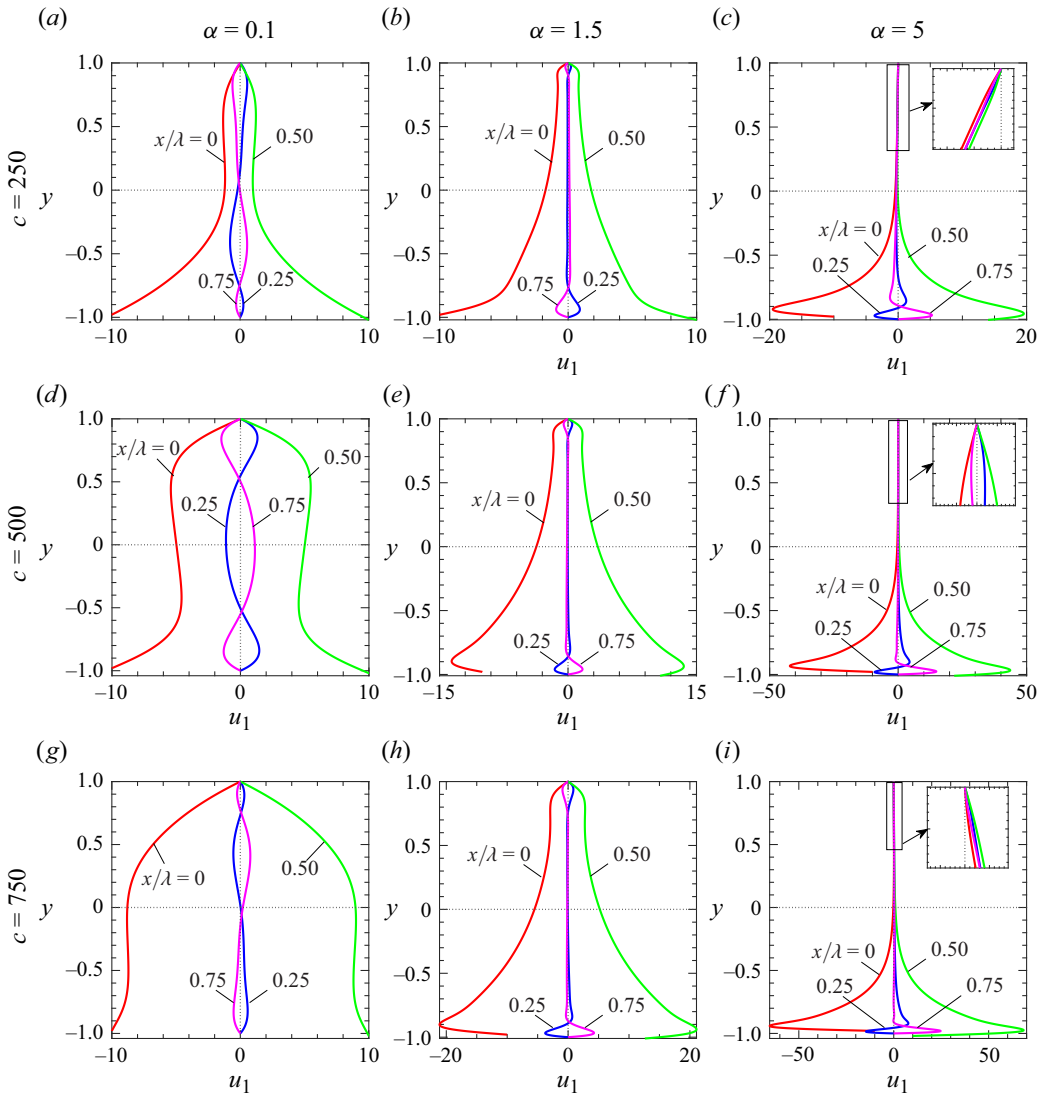
Figure 3. Distributions of the x-component of the vibrations-induced velocity modifications $u_{1,B}$ at $x/\lambda = 0, 0.25, 0.5, 0.75$ for $Re = 1000$, $A = 0.04$.

Unsteady three-dimensional disturbances are added to the stationary state in the form

$$\boldsymbol{\omega} = \boldsymbol{\omega}_B (x, y) + \boldsymbol{\omega}_D (x, y, z, t), \quad \boldsymbol{V} = \boldsymbol{V}_B (x, y) + \boldsymbol{V}_D (x, y, z, t), \quad (4.2a,b)$$

where subscript D denotes disturbance quantities, $\boldsymbol{\omega}_D = (\xi_D, \eta_D, \phi_D)$, $\boldsymbol{V}_D = (u_D, v_D, w_D)$, the flow quantities (4.2) are substituted into (4.1), the base part is subtracted, and the equations are linearised. The resulting linear disturbance equations have the form

$$\frac{\partial \boldsymbol{\omega}_D}{\partial t} - (\boldsymbol{\omega}_B . \boldsymbol{\nabla}) \, \boldsymbol{V}_D - (\boldsymbol{\omega}_D . \boldsymbol{\nabla}) \, \boldsymbol{V}_B + (\boldsymbol{V}_B . \boldsymbol{\nabla}) \, \boldsymbol{\omega}_D + (\boldsymbol{V}_D . \boldsymbol{\nabla}) \, \boldsymbol{\omega}_B - c \frac{\partial \boldsymbol{w}_D}{\partial x} = \boldsymbol{\nabla}^2 \boldsymbol{\omega}_D,$$

$$(4.3a)$$

$$\boldsymbol{\nabla} . \boldsymbol{V}_D = 0, \quad \boldsymbol{\omega}_D = \boldsymbol{\nabla} \times \boldsymbol{V}_D, \quad (4.3b,c)$$

$$\text{for } y = 1,\, y_L(x), \quad \boldsymbol{V}_D(x, y, z, t) = 0. \tag{4.3d}$$

Since vibrations modulate the stationary state, the disturbance quantities can be expressed as waves with amplitudes modulated in the x-direction (Floryan 1997), i.e.

$$[\boldsymbol{V}_D, \boldsymbol{\omega}_D]\,(x, y, z, t) = [\boldsymbol{G}_D, \boldsymbol{\Omega}_D]\,(x, y)\, e^{i(\delta x + \mu z - \sigma t)} + \text{c.c.}, \tag{4.4a}$$

where δ and μ are the real wavenumbers in the x- and z-directions, respectively, $\sigma = \sigma_r + i\sigma_i$ is the complex frequency with σ_i describing the rate of growth of disturbances and σ_r describing their frequency, and c.c. stands for the complex conjugate. The amplitude functions $\boldsymbol{G}_D(x, y)$ and $\boldsymbol{\Omega}_D(x, y)$ are x-periodic as dictated by the type of modulation. Accordingly, these functions can be expressed in terms of Fourier expansions of the form

$$\boldsymbol{G}_D\,(x, y) = \sum_{m=-N_D}^{+N_D} [g_u^{<m>}\,(y)\,,\, g_v^{<m>}\,(y)\,,\, g_w^{<m>}\,(y)]\, e^{im\alpha x} + \text{c.c.}, \tag{4.5a}$$

$$\boldsymbol{\Omega}_D\,(x, y) = \sum_{m=-N_D}^{+N_D} [g_\xi^{<m>}\,(y)\,,\, g_\eta^{<m>}\,(y)\,,\, g_\phi^{<m>}\,(y)]\, e^{im\alpha x} + \text{c.c.}. \tag{4.5b}$$

Quantities in square brackets on the right-hand sides of (4.5) are the modal functions. Combining (4.4) and (4.5) leads to the final expressions for the disturbance quantities in the form

$$\boldsymbol{V}_D(x, y, z, t) = \sum_{m=-N_D}^{+N_D} \left[g_u^{<m>}(y),\, g_v^{<m>}(y),\, g_w^{<m>}(y) \right] e^{i[(\delta+m\alpha)x + \mu z - \sigma t]} + \text{c.c.}, \tag{4.6a}$$

$$\boldsymbol{\omega}_D\,(x, y, z, t) = \sum_{m=-N_D}^{+N_D} \left[g_\xi^{<m>}\,(y)\,,\, g_\eta^{<m>}\,(y)\,,\, g_\phi^{<m>}\,(y) \right] e^{i[(\delta+m\alpha)x + \mu z - \sigma t]} + \text{c.c.}. \tag{4.6b}$$

Substituting (4.6) into (4.3a–c) and separating Fourier modes leads to a system of coupled ordinary differential equations for the modal functions. These equations are then combined into a system involving only $g_v^{<m>}$ and $g_\eta^{<m>}$ in the form

$$T^{<m>} g_v^{<m>} = - \sum_{n=-N_D}^{N_D} \left[(T_1^{<m-n>} + T_2^{<m-n>} + T_3^{<m-n>}) g_v^{<m-n>} \right.$$
$$\left. + \left(T_4^{<m-n>} - T_5^{<m-n>} \right) g_\eta^{<m-n>} \right], \tag{4.7a}$$

$$S^{<m>} g_\eta^{<m>} = \sum_{n=-N_D}^{+N_D} \left[\left(S_1^{<m-n>} + S_2^{<m-n>} + S_3^{<m-n>} \right) g_v^{<m-n>} \right.$$
$$\left. + \left(S_4^{<m-n>} - S_5^{<m-n>} \right) g_\eta^{<m-n>} \right], \tag{4.7b}$$

where $N_D \le m \le -N_D$, and all operators are defined in Appendix B.

The boundary conditions for the modal functions at the upper plate follow from (4.3*d*) and have a simple form, i.e.

$$\text{for } y = 1, \quad g_u^{<m>} = g_v^{<m>} = g_w^{<m>} = 0, \tag{4.8}$$

and when expressed only in terms of $g_v^{<m>}$ and $g_\eta^{<m>}$, they take the form

$$\text{for } y = 1, \quad \mathrm{i}t_m \mathrm{D}g_v^{<m>} - \mathrm{i}\mu g_\eta^{<m>} = g_v^{<m>} = \mathrm{i}\mu \mathrm{D}g_v^{<m>} + \mathrm{i}t_m g_\eta^{<m>} = 0. \tag{4.9}$$

The boundary conditions at the lower plate involve a combination of modes dictated by the plate geometry. They can be written as

$$\text{for } y = y_L(x), \quad \sum_{m=-N_D}^{N_D} g_u^{<m>} \, \mathrm{e}^{\mathrm{i}m\alpha x} = 0, \quad \sum_{m=-N_D}^{N_D} g_v^{<m>} \, \mathrm{e}^{\mathrm{i}m\alpha x} = 0, \quad \sum_{m=-N_D}^{N_D} g_w^{<m>} \, \mathrm{e}^{\mathrm{i}m\alpha x} = 0, \tag{4.10a–c}$$

and, when expressed in terms of $g_v^{<m>}$ and $g_\eta^{<m>}$, they take the form

$$\text{for } y = y_L(x), \quad \sum_{m=-N_D}^{N_D} [-\mathrm{i}\mu g_\eta^{<m>} + \mathrm{i}t_m \mathrm{D}g_v^{<m>}] \, \mathrm{e}^{\mathrm{i}m\alpha x} = 0, \quad \sum_{m=-N_D}^{N_D} g_v^{<m>} \, \mathrm{e}^{\mathrm{i}m\alpha x} = 0, \tag{4.11a,b}$$

$$\sum_{m=-N_D}^{N_D} [\mathrm{i}t_m g_\eta^{<m>} + \mathrm{i}\mu \mathrm{D}g_v^{<m>}] \, \mathrm{e}^{\mathrm{i}m\alpha x} = 0. \tag{4.11c}$$

These conditions are replaced by constraints whose form suitable for numerical implementation is dictated by the discretisation applied to (4.7).

The discretisation of (4.7) relies on Chebyshev expansions, with the first step involving transformation (3.6) so that a standard definition of Chebyshev expansions can be used. The modal functions were represented as Chebyshev expansions, i.e.

$$q_D^{(m)}(\hat{y}) = \sum_{k=0}^{N_{K-1}} Gq_{k,D}^{(m)} \, T_k(\hat{y}), \tag{4.12}$$

where $q_D^{(m)}(\hat{y})$ stands for any of the modal functions, and $Gq_{k,D}^{(m)}$ are the unknown expansion coefficients. The complete discretisation procedure involving a combination of (4.7), (4.9), and (4.11) provides spectral accuracy. The immersed boundary conditions method was used to discretise (4.11). Details are omitted from this presentation due to their length, but can be found in Panday & Floryan (2023). The use of the Galerkin projection method combined with the tau procedure (Canuto *et al.* 1992) for incorporation of the boundary conditions led to an eigenvalue problem for a very large system of linear algebraic equations for the unknowns $Gq_{k,D}^{(m)}$. The solution procedure and its accuracy testing are described in Panday & Floryan (2023). All eigenvalues presented in the discussion below were determined with an accuracy of no less than four digits.

5. Discussion of results

Secondary structures in the form of vortices are aligned with the flow direction with their spanwise size given by the spanwise wavenumber μ. These vortices are modulated by the spatial form of vibrations, which means that their modulation is characterised by
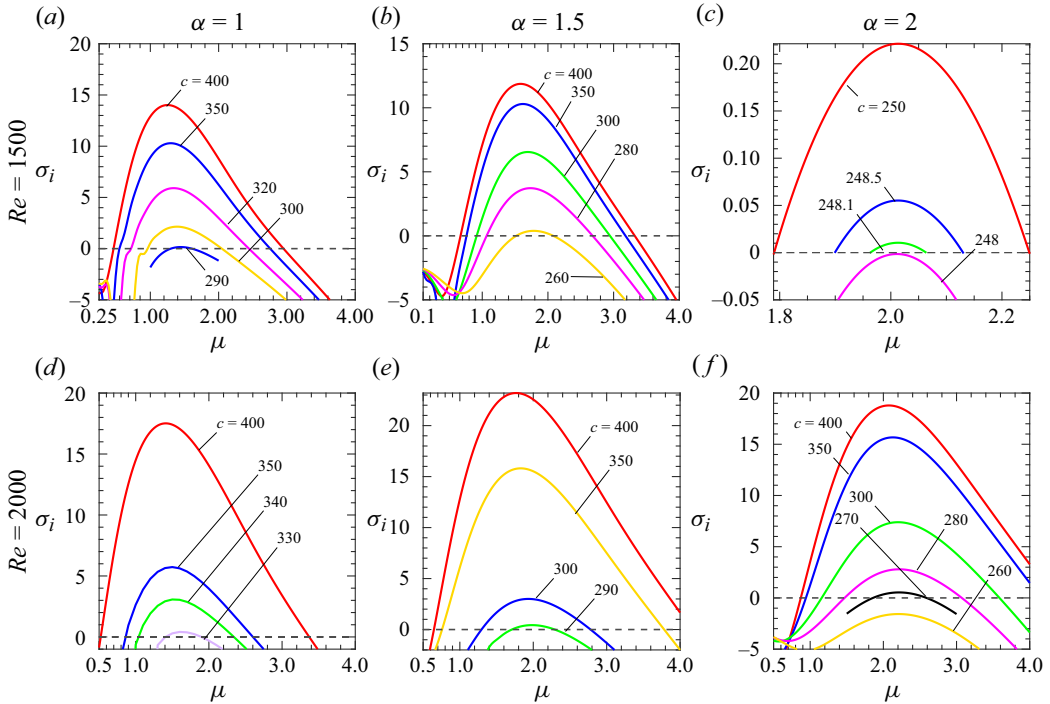
Figure 4. Variations of the amplification rate σ_i as a function of the vortex wavenumber μ for selected flow Reynolds numbers Re, wavenumber α, and wave phase speeds c.

the wavenumber α. Our first set of results pertains to the amplification of vortex-type disturbances as a function of μ. The growth rates are shown in figure 4 for those waves that are the most effective in producing instability (we return to this point later). Amplification of the modes is possible only if the phase speed of the vibration is sufficiently large, and our calculations show that the phase speed needs to reach at least $c \approx 300$. Our calculations also show that vortices with wavenumbers in the interval $\mu \approx 1-2$ seem to be the most likely to emerge.

The critical Reynolds number required for instability depends on both α and c; typical results are depicted in figure 5(a). There is an absolute minimal phase speed required to produce instability – it is $c = 406.4, 260.5, 248.8, 248.1$ for $\alpha = 0.3, 1, 1.5, 2$. This minimal phase speed increases with the Reynolds number, as documented in figure 6. The results presented in figure 6 are for $Re = 980, 1005, 1230, 1500$, which are Reynolds numbers producing instability for the smallest c for $\alpha = 0.3, 1, 1.5, 2$, respectively. There is no upper limit on the phase speed producing instability, but Re_{cr} increases nearly linearly with c at large values of c (see figure 5a). It is clear that waves with phase speed $c \approx 300-500$ lead to the smallest Re_{cr}. The minimum Re_{cr} depends on the wave wavelength, and it is $Re_{cr} = 884.6, 737, 1025.5, 1298.5$ for $\alpha = 0.3, 1, 1.5, 2$.

The vortex properties corresponding to critical conditions exhibit complex behaviour. In general, μ_{cr} increases with an increase of α. Variations of μ_{cr} as a function of c exhibit a local minimum around $c \approx 400$ for all α; however, an increase of c away from this minimum leads to an increase of μ_{cr} for midrange α ($\alpha = 1, 1.5$) and a decrease for small ($\alpha = 0.3$) and large ($\alpha = 2$) values, as illustrated in figure 5(b).

The fact that the wave is required to have a certain minimum phase speed before it can destabilise the flow is further illustrated in figure 6. Here, it is seen that a small increase
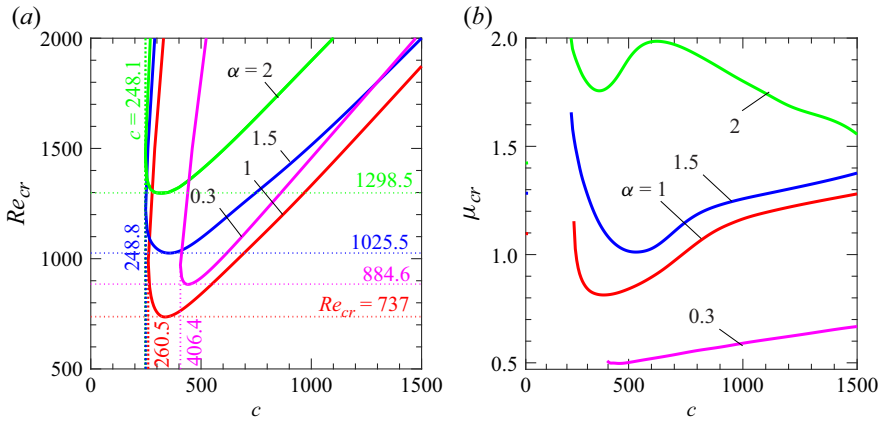
Figure 5. Variations of (*a*) the critical Reynolds number Re_{cr}, and (*b*) the critical wavenumber μ, as functions of the wave phase speed c for the wave with amplitude $A = 0.06$ and selected wavenumbers α. The vertical dotted lines in (*a*) show the minimum wave speed required to initiate the instability. The horizontal dotted lines show the minimum critical Reynolds number Re_{cr} for all phase speeds c.
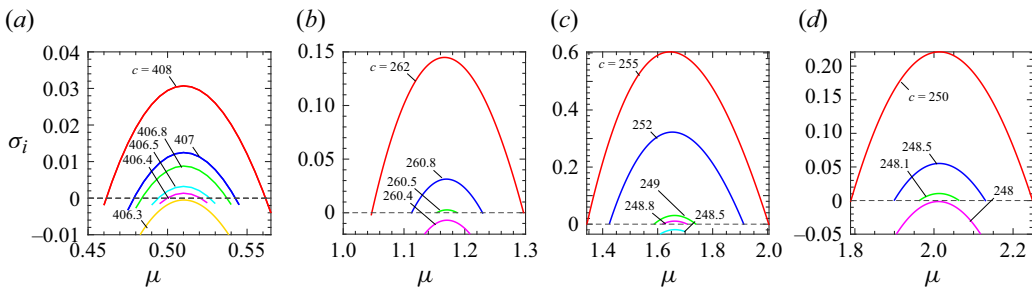

Figure 6. Variations of the amplification rate σ_i as a function of the phase speed c for waves with amplitude $A = 0.06$ and (*a*) $(\alpha, Re) = (0.3, 980)$, (*b*) $(\alpha, Re) = (1, 1005)$, (*c*) $(\alpha, Re) = (1.5, 1230)$, (*d*) $(\alpha, Re) = (2, 1500)$.

of c above its minimum value leads to a relatively rapid increase in the amplification rate, and a significant widening in the vortex wavenumber μ range that is unstable. One may speculate that once the flow becomes susceptible to this form of instability, a wide range of vortex sizes may plausibly emerge.

The next two figures concern the structure of the curves that identify neutrally stable modes. First, figure 7 shows the form of these curves in the (μ, Re)-plane for a selection of vibration wavenumbers α; the companion plot in figure 8 displays similar data but for a few phase speeds c.

Given a certain wave speed, there is the most effective wavenumber leading to the lowest Re_{cr}. When $c = 300, 400, 500$, the most effective α is always $\alpha \approx 0.7$, leading to $Re_{cr} = 680, 700, 790$, respectively (see figure 8), producing vortices with similar wavenumbers, i.e. $\mu \approx 0.75$. When $\alpha = 1, 1.5, 2$, there is the most effective phase speed, and it is $c = 350, 350, 300$ for $\alpha = 1, 1.5, 2$, with critical vortex wavenumber $\mu_{cr} \approx 0.85, 1.2, 1.85$, respectively (see figure 7). All these data demonstrate the existence of the most effective wavenumber and wave phase speed leading to the smallest Re_{cr}.

We deduce from figures 5 and 6 that small changes in the vibration wave characteristics can significantly alter the corresponding Re_{cr}. The resulting vortex size, as measured by μ_{cr}, changes only marginally with c, but is much more sensitive to the precise value of α.
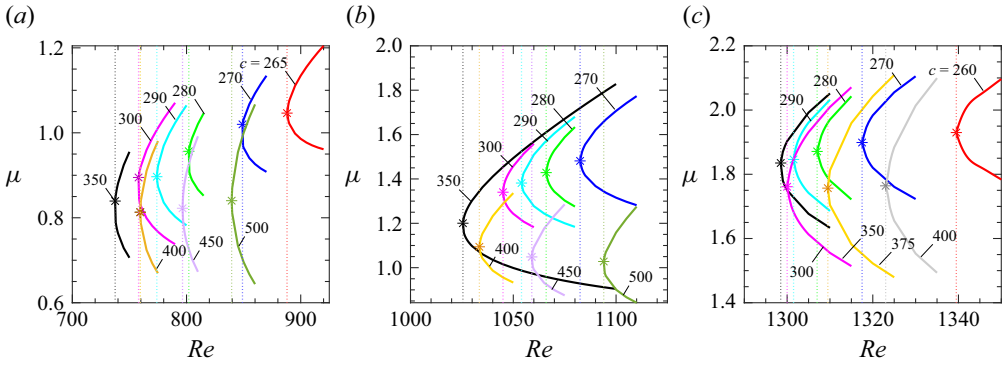
Figure 7. Neutral curves in the (μ, Re)-plane for $A = 0.06$ and (*a*) $\alpha = 1$, (*b*) $\alpha = 1.5$, (*c*) $\alpha = 2$. Stars identify the critical Reynolds number Re_{cr} and the critical vortex wavenumber μ_{cr}.
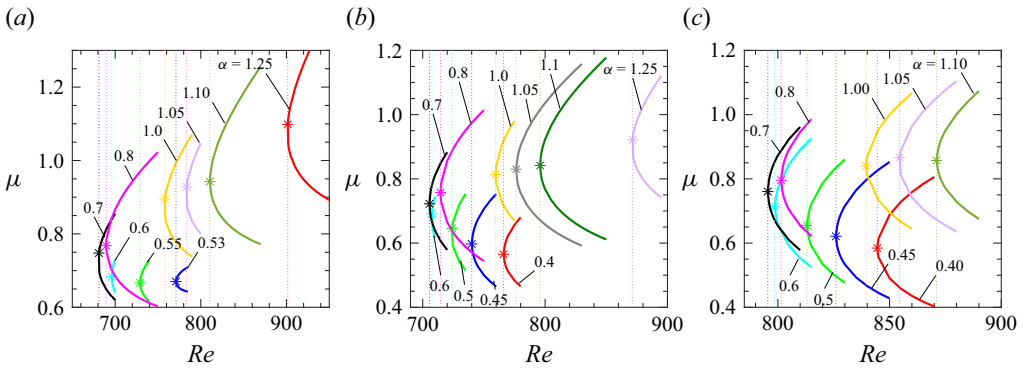

Figure 8. Neutral curves in the (μ, Re)-plane for $A = 0.06$ and (*a*) $c = 300$, (*b*) $c = 400$, (*c*) $c = 500$. Stars identify the critical Reynolds number Re_{cr} and the critical vortex wavenumber μ_{cr}.
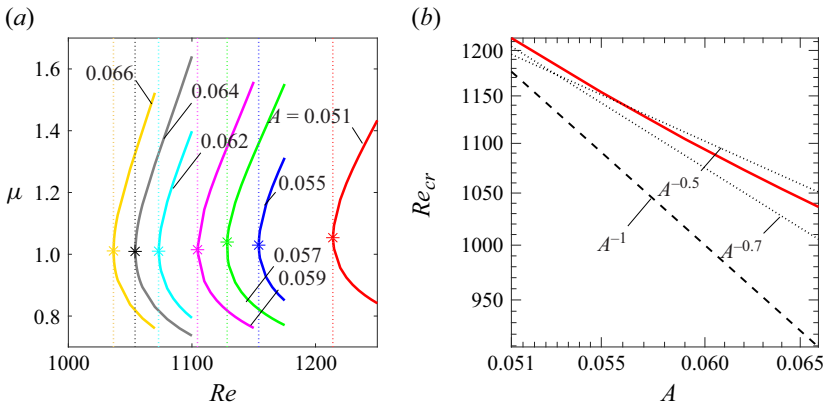

Figure 9. (*a*) Neutral curves in the (μ, Re)-plane for different A values. Stars identify the critical Reynolds number Re_{cr} and the critical vortex wavenumber μ_{cr}. (*b*) Variations of the critical Reynolds number Re_{cr} as a function of wave amplitude A. All results are for $\alpha = 1.5$, $c = 500$.

The effects of the changes in the wave amplitude are considered in figure 9. The critical Reynolds number decreases with larger vibrations A, and seems to grow proportional to $A^{-2/3}$ as $A \rightarrow 0$. It would be interesting to show theoretically that this is indeed the case, but such detailed asymptotic work is deferred to later study.
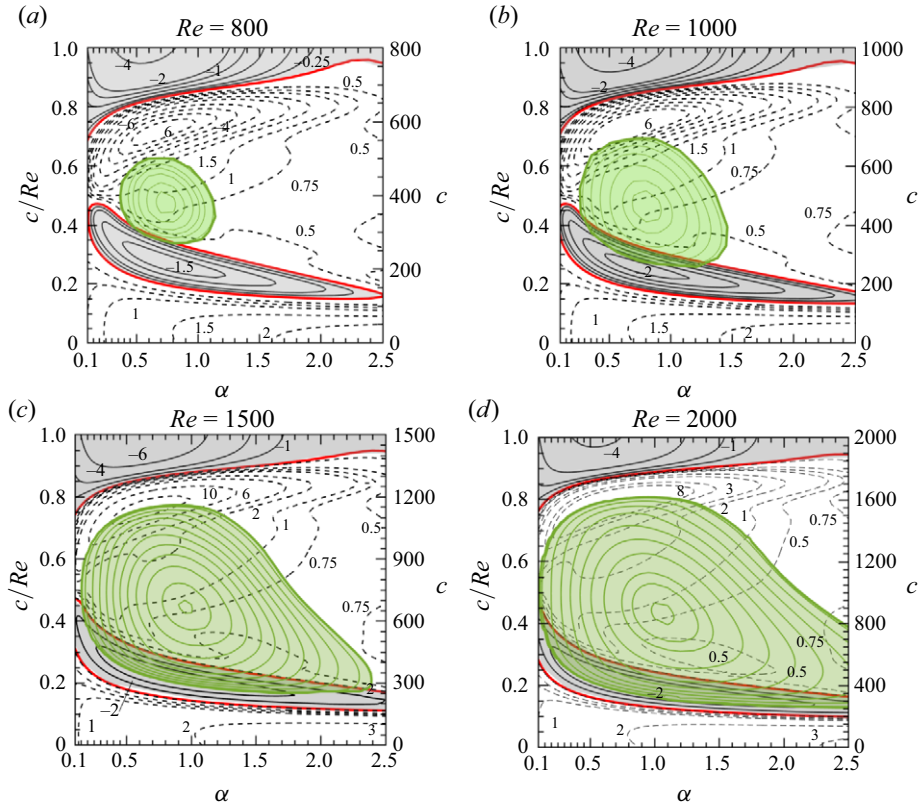
1006 A25-14

Figure 10. Zones of instability (marked in green) in the (α, c)-plane for the wave amplitude $A = 0.06$. The background shows variations in the normalised force correction $F_{norm} = F_{1,B}/(Re\, F_0 A^2)$; the grey shading indicates negative F_{norm}, while the red line shows $F_{norm} = 0$.

All the information relating to the instability can be combined to give an overall picture of the flow characteristics. The results in figure 10 include convincing evidence that only subcritical waves can produce vortex instability. The range of wave phase speeds leading to destabilisation expands as Re grows; however, they are always subcritical and cannot propagate against the flow. As the range of phase speeds expands, so too does the interval of vibration wavenumbers. Of particular interest in connection with figure 10 is the region of parameter space where the green- and grey-shaded zones overlap. Those pairs of α and c that lie in this common zone identify vibration waves that can reduce flow losses while simultaneously creating vortices through destabilisation. These waves are obviously of great interest in mixed intensification.

5.1. *Disturbance properties and instability characteristics*

We will now probe the disturbance properties and instability characteristics in greater detail. We begin with figure 11, which displays the disturbance spectra that identify the unstable modes. These modes have zero frequency, demonstrating that they do not propagate and can be identified as streamwise vortices. They can be connected to the Squire spectrum in the infinitesimal amplitude limit $A \to 0$, as demonstrated by the data shown in figure 12. Moreover, these results confirm that wave amplitude A must exceed a certain minimum size before instability may occur, and that there is a finite range of wave phase speeds c over which the flow is destabilised.
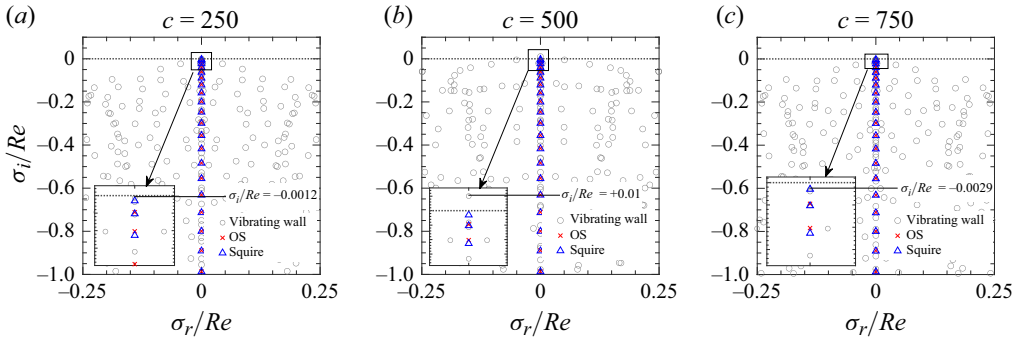
Figure 11. Spectra for $Re = 1000$, $A = 0.08$, $\alpha = 0.7$, $\mu = 0.7$, $\delta = 0$. The labels OS and Squire identify the Orr–Somerfield and Squire modes.

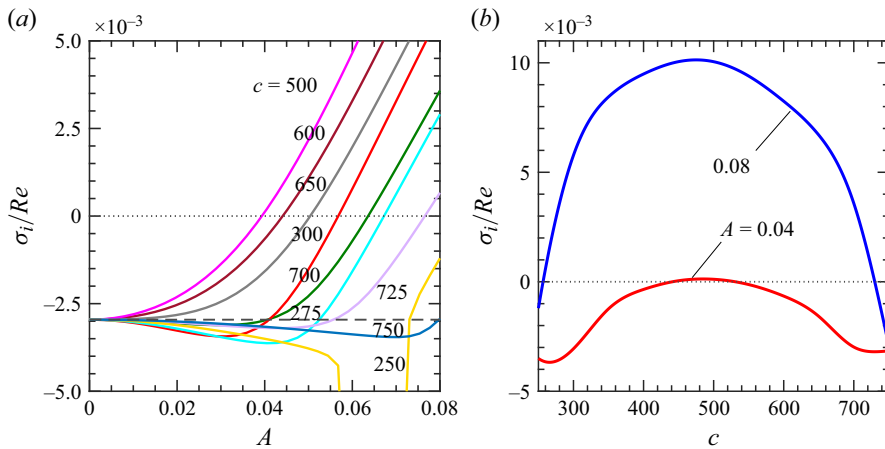Figure 12. Variations of the amplification rate σ_i/Re (*a*) as a function of the wave amplitude A, and (*b*) as a function of the wave phase speed c, for $Re = 1000$, $\alpha = 0.7$, $\mu = 0.7$, $\delta = 0$. The horizontal dashed line in (*a*) corresponds to the least attenuated Squire mode of Couette flow.

The topology of the disturbance velocity field can be inferred from the plots of eigenfunctions displayed in figure 13. This structure is characteristic of streamwise vortices in shear layers. Vibrations produce vortices in cross-planes, which transport low-speed fluid away from the wall (upwash) and high-speed fluid towards the wall (downwash), thereby creating longitudinal streaks (Floryan 1991). The disturbance velocity field is dominated by mode $n = 0$, representing the vortex motion, while higher-order modes represent streamwise modulation of this vortex. In particular, we note that the mode shapes $g_u^{(0)}$ and $g_v^{(0)}$ are purely real, and $g_w^{(0)}$ is purely imaginary, while the remaining modes are complex. The rotational movement exhibited by v_D and w_D is quite weak but is sufficient to result in a large defect in the streamwise velocity distribution. That this is the case is confirmed by the observation that the mode $g_u^{(0)}$ is roughly an order of magnitude larger than either $g_v^{(0)}$ or $g_w^{(0)}$. The disturbance velocity field comprises two layers of vortices when $c = 250$ (the first row in figure 13) and one layer when $c = 500$ (the second row) but reverts to two layers again once $c = 750$ (the third row). The structure of $g_u^{(0)}$ displayed in figure 14(*a*) illustrates these transitions as c increases. The maximum of $g_u^{(0)}$ is close to the vibrating wall when the phase speed is small; the velocity field comprises two layers
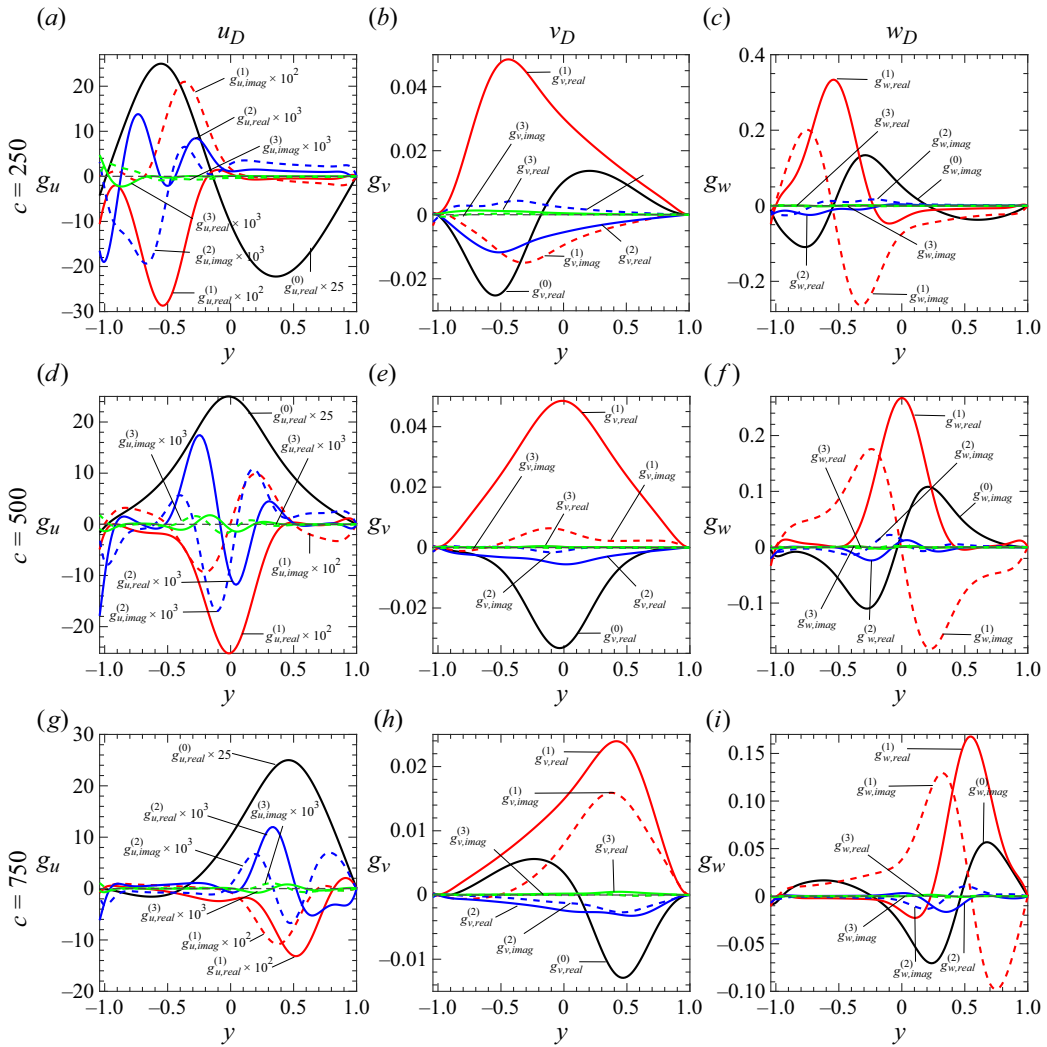
1006 A25-16

Figure 13. Distributions of the three leading ($n = 0, 1, 2$) eigenfunctions for the disturbance velocity components for the wave amplitude $A = 0.08$, wavenumber $\alpha = 0.7$, flow Reynolds number $Re = 1000$, and vortex wavenumber $\mu = 0.7$.

of vortices, and the flow is stable. As c increases, the principal zone of intense activity shifts towards the middle of the slot; the flow field now consists of only a single layer of vortices, and the flow is unstable. Further increase of c moves the activity zone towards the smooth plate; the flow field consists of two layers of vortices, and the flow becomes stable again. The change from one layer of vortices to two layers tends to increase the velocity gradients, enhancing the dissipation, and is conducive to flow stabilisation.

A characteristic flow field topology associated with unstable vortices is illustrated in figure 15. The structure of the disturbance velocity field corresponding to unstable vortices is independent of the wavenumber α (see figures 16a,b). The centre of the vortex moves closer to the vibrating wall as Re increases, and the disturbance velocity field eventually splits into two layers of vortices, with the primary vortex near the vibrating wall being directly driven by the instability (figures 16c,d).
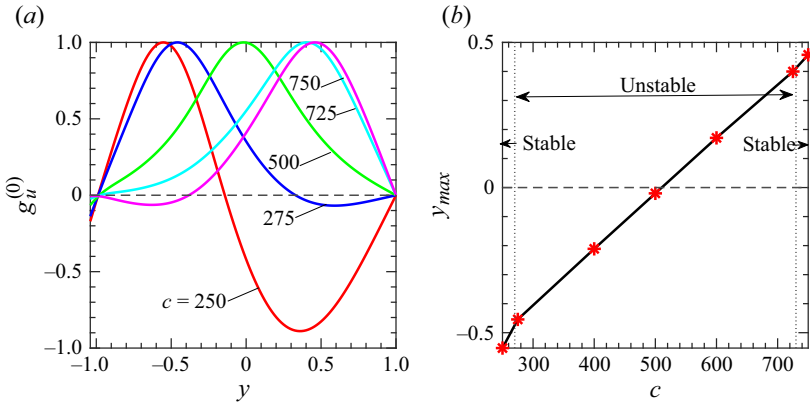
Figure 14. (*a*) Distributions of mode zero $g_u^{(0)}$ of the x-component of the disturbance velocity vector, and (*b*) variations of the position y_{max} of the maximum of $g_u^{(0)}$ as a function of the wave phase speed c for the wave amplitude $A = 0.08$, wavenumber $\alpha = 0.7$, flow Reynolds number $Re = 1000$, and vortex wavenumber $\mu = 0.7$. Thin dotted vertical lines in (*b*) show the neutral stability conditions.

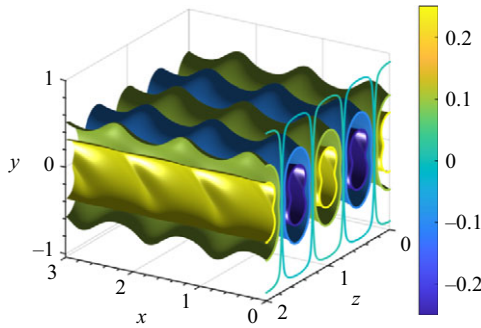Figure 15. Contour plot of the streamwise disturbance velocity component u_D for the wave amplitude $A = 0.08$, wavenumber $\alpha = 0.7$, wave speed $c = 500$, flow Reynolds number $Re = 1000$, and vortex wavenumber $\mu = 0.7$.

Finally, we point out that the vortices' streaks are susceptible to instabilities (Park, Hwang & Cossu 2011). If these occur, then they may lead to either optimal roll structures that maximise the transient temporal growth of the streaks (Schmid & Henningson 2001) or asymptotic growth in the form of normal modes leading to secondary instabilities (Floryan 1991).

6. Energy analysis

Further information concerning the properties of the flow can be gleaned by considering the form of the energy transfer between the base flow and the disturbances. To explore this, we can start with the field equations expressed in terms of primitive variables, i.e.

$$\frac{\partial \boldsymbol{V}}{\partial t} + \boldsymbol{V}.\boldsymbol{\nabla}\boldsymbol{V} + \boldsymbol{\nabla}p = \boldsymbol{\nabla}^2\boldsymbol{V}, \quad \boldsymbol{\nabla}.\boldsymbol{V} = 0. \tag{6.1a,b}$$

The variables are separated into the basic state plus the disturbances, so that

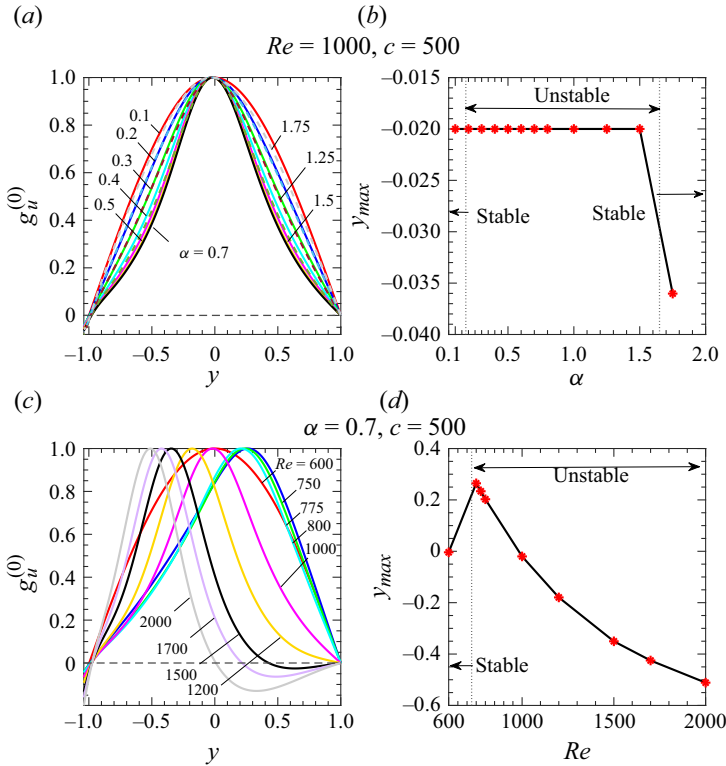$$\boldsymbol{V} = \boldsymbol{V}_B + \boldsymbol{v}_D, \quad p = p_B + p_D. \tag{6.2a,b}$$

Figure 16. Distributions of mode zero $g_u^{(0)}$ of the x-component of the disturbance velocity vector, and variations of locations of their maxima, as functions of (a,b) the wavenumber α, and (c,d) the Reynolds number Re. All results are for the vortex wavenumber $\mu = 0.7$ and the wave amplitude $A = 0.08$.

Substitution of (6.2) into (6.1) and linearisation show that

$$\frac{\partial \boldsymbol{v}_D}{\partial t} + \boldsymbol{V}_B.\boldsymbol{\nabla}\boldsymbol{v}_D + \boldsymbol{v}_D.\boldsymbol{\nabla}\boldsymbol{V}_B + \boldsymbol{\nabla}p_D = \boldsymbol{\nabla}^2\boldsymbol{v}_D, \quad \boldsymbol{\nabla}.\boldsymbol{v}_D = 0. \tag{6.3}$$

An appropriate mechanical energy functional can be constructed by taking the scalar product of the momentum equation with the disturbance velocity vector. The result is then integrated over a control volume that extends across the channel and over one wavelength in the x- and z-directions. This gives (in index notation)

$$\int_{-1}^{1} \int_{0}^{\lambda_z} \int_{0}^{\lambda_x} \left(\frac{1}{2}\frac{\partial}{\partial t}\left(v_{D,i}v_{D,i}\right) + v_{D,i}V_{B,j}\frac{\partial v_{D,i}}{\partial x_j} + v_{D,i}v_{D,j}\frac{\partial V_{B,i}}{\partial x_j} + v_{D,i}\frac{\partial p_D}{\partial x_i} \right) \mathrm{d}x\,\mathrm{d}z\,\mathrm{d}y$$
$$= \int_{-1}^{1} \int_{0}^{\lambda_z} \int_{0}^{\lambda_x} \left(\boldsymbol{\nabla}^2 v_{D,i} \right).v_{D,i}\,\mathrm{d}x\,\mathrm{d}z\,\mathrm{d}y. \tag{6.4}$$

The application of periodicity conditions and Green's theorem leads to

$$\lambda_x^{-1}\lambda_z^{-1} \int_{-1}^{1} \int_{0}^{\lambda_z} \int_{0}^{\lambda_x} \frac{1}{2}\frac{\partial}{\partial t}\left(v_{D,i}v_{D,i}\right)\mathrm{d}x\mathrm{d}z\mathrm{d}y$$
$$= -\lambda_x^{-1}\lambda_z^{-1} \int_{-1}^{1} \int_{0}^{\lambda_z} \int_{0}^{\lambda_x} \frac{\partial v_{D,i}}{\partial x_j}\frac{\partial v_{D,i}}{\partial x_j}\mathrm{d}x\mathrm{d}z\mathrm{d}y$$
$$- \lambda_x^{-1}\lambda_z^{-1} \int_{-1}^{1} \int_{0}^{\lambda_z} \int_{0}^{\lambda_x} v_{D,i}v_{D,j}\frac{\partial V_{B,i}}{\partial x_j}x\mathrm{d}z\mathrm{d}y \tag{6.5}$$

	Integration interval	I_{kin}	I_1	I_2	I_3	I_4	$I_{inertia}$
$c = 250$	$0 < x < \lambda/2$	-0.0371	0.0489	-0.3753	0.0012	-1.479×10^{-4}	-0.3252
	$\lambda/2 < x < \lambda$	-0.0484	-0.0766	-0.5153	0.0025	2.158×10^{-4}	-0.5892
	$0 < x < \lambda$	-0.0855	-0.0277	-0.8906	0.0038	6.795×10^{-5}	-0.9144
$c = 500$	$0 < x < \lambda/2$	0.6508	0.2382	-1.3603	0.0124	-0.0011	-1.1107
	$\lambda/2 < x < \lambda$	0.6567	-0.2291	-0.9803	0.0116	8.474×10^{-4}	-1.1969
	$0 < x < \lambda$	1.3076	0.009	-2.3406	0.0241	-2.789×10^{-4}	-2.3076
$c = 750$	$0 < x < \lambda/2$	-0.1977	0.3665	-0.9492	0.0055	-6.383×10^{-4}	-0.5777
	$\lambda/2 < x < \lambda$	-0.1453	-0.2427	0.1596	0.0036	4.217×10^{-4}	-0.0790
	$0 < x < \lambda$	-0.3431	0.1237	-0.7896	0.0091	-2.166×10^{-4}	-0.6568

Table 1. Elements of the energy integral for $A = 0.08$, $Re = 1000$, $\alpha = 0.7$, $\mu = 0.07$.

where the factor $\lambda_x^{-1}\lambda_z^{-1}$ is included to demonstrate that all quantities are evaluated per unit length in the x- and z-directions. The first term on the right-hand side of this balance describes dissipation, which is always positive, with the normalisation of the disturbance velocity field chosen to make this integral unity. The normalised energy relation then becomes

$$
\lambda_x^{-1}\lambda_z^{-1} \int_{-1}^{1} \int_0^{\lambda_z} \int_0^{\lambda_x} \frac{1}{2} \frac{\partial}{\partial t} \left(v_{D,i} v_{D,i} \right) \, dx \, dz \, dy
$$
$$
= -1 - \lambda_x^{-1}\lambda_z^{-1} \int_{-1}^{1} \int_0^{\lambda_z} \int_0^{\lambda_x} v_{D,i} v_{D,j} \frac{\partial V_{B,i}}{\partial x_j} \, dx \, dz \, dy. \tag{6.6}
$$

The left-hand side (I_{kin}) denotes the rate of growth of kinetic energy of disturbances. This energy increases with time if the second term on the right-hand side, which captures the inertial effects ($I_{inertia}$), dominates over the dissipation. This occurs when $I_{inertia} < -1$. The identification of elements of the base flow responsible for the instability requires an explicit decomposition of the inertial integral so that

$$
I_{inertia} = \lambda_x^{-1}\lambda_z^{-1} \int_{-1}^{1} \int_0^{\lambda_z} \int_0^{\lambda_x} \left(u_D u_D \frac{\partial u_B}{\partial x} + u_D v_D \frac{\partial u_B}{\partial y} + v_D u_D \frac{\partial v_B}{\partial x} + v_D v_D \frac{\partial v_B}{\partial y} \right)
$$
$$
\times \, dx \, dz \, dy = I_1 + I_2 + I_3 + I_4. \tag{6.7}
$$

Integration in the x-direction was divided into two parts to enable easy identification of those contributions ascribed to effects of the downwelling and those corresponding to the upwelling parts of the wave. Some typical results are summarised in table 1. These demonstrate that $\partial u_B / \partial y$ combined with Reynolds stresses is mainly responsible for the energy transfer to the disturbances, with other terms having an almost negligible effect. The upwelling and downwelling parts of the wave contribute similar amounts to the energy transfers. The inertial terms have insufficient strength to overcome dissipation when $c = 250$ and $c = 750$, but can do it when $c = 500$. When this happens, the Reynolds stress is responsible for the energy transfer.

A qualitative analysis of the energy transfers aids insight into the flow dynamics. The reference flow dominates the primary state as the vibration-created flow modifications are at least an order of magnitude smaller, as was seen in figure 3. This means that

$$
u_B \approx Re\, u_0\,(y), \quad \frac{\partial u_B}{\partial y} \approx \frac{1}{2}\, Re, \quad v_B \approx 0, \quad \frac{\partial u_B}{\partial x} \approx \frac{\partial v_B}{\partial x} \approx \frac{\partial v_B}{\partial y} \approx 0. \tag{6.8a–d}
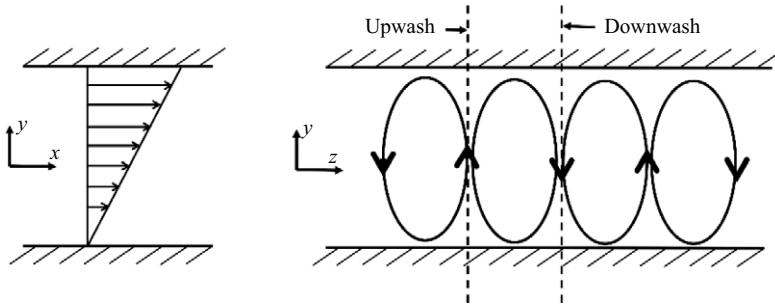$$

Figure 17. Sketch of the unstable fluid movement.

The disturbance velocity field is dominated by mode zero, as portrayed in figure 13. This means that

$$u_D(x, y, z) \approx g_u^{\langle 0 \rangle}(y)e^{i\mu z} + g_u^{\langle 0 \rangle}(y)e^{-i\mu z} = 2g_u^{\langle 0 \rangle}(y)\cos(\mu z), \qquad (6.9a)$$

$$v_D(x, y, z) \approx g_v^{\langle 0 \rangle}(y)e^{i\mu z} + g_v^{\langle 0 \rangle}(y)e^{-i\mu z} = 2g_v^{\langle 0 \rangle}(y)\cos(\mu z). \qquad (6.9b)$$

Energy integrals I_1, I_3, I_4 can be neglected, and I_2 can be approximated as

$$I_2 = Re \int_{-1}^{1} g_u^{\langle 0 \rangle} g_v^{\langle 0 \rangle} \mathrm{d}y. \qquad (6.10)$$

This integral must be sufficiently negative to enable growth in the disturbance energy. This is possible only if the *x*- and *y*-disturbance velocity components are out of phase, which indeed is the case as illustrated in the eigenfunctions displayed in figure 13. The phase difference between u_D and v_D can be explained with the help of the sketch displayed in figure 17. Vortex motions in the downwash zone have a negative v_D that brings high-velocity fluid closer to the lower plate and generates a positive u_D. The product $v_D u_D$ is therefore negative, which is the necessary condition to maintain the instability.

Experimental verification of the above predictions would be desired. Theoretically, at least, one could create well-controlled surface vibrations using a system of piezoelectric pistons turned on and off in a proper sequence to produce surface waves with the desired wavelength and phase speeds. However, this description is somewhat over-simplistic, for it should be recognised that many practical difficulties are associated with constructing such a system. Practical progress is likely to be slow.

7. Summary

This study shows how vibrations applied to a bounding plate can transform the otherwise linearly stable Couette flow into a form susceptible to instability. Appropriately applied vibrations may reduce flow resistance; supercritical waves, i.e. those faster than the flow, always reduce losses. In contrast, the situation for subcritical waves is somewhat more involved and can be determined only after more careful analysis. The vibrations can also lead to instability, and constitute a mechanism capable of generating a secondary flow that manifests as streamwise vortices. If the physical properties of the vibration waves are tuned properly, then instability may set in at a fluid Reynolds number as small as a few hundred. The instability is driven by centrifugal forces created by the wave-imposed changes in the direction of fluid movement, and the process is operative as long as the vibrations are

of sufficient size. The disturbance velocity field is characterised by a streamwise velocity component larger than the wall-normal and spanwise components. The resulting streaks are expected to initiate a travelling wave instability driven by an inviscid mechanism associated with inflection points in the distribution of the spanwise velocity component. Such an instability can ultimately lead to Lagrangian chaos.

Surface vibrations may arise as an uncontrolled effect or be introduced intentionally. The calculations described herein form a basis that may guide how the effects of uncontrolled vibrations may be assessed. Such disturbances have the undesirable property that they may prove capable of initiating processes that eventually lead to a premature transition to turbulence.

The mechanisms described here are inherently somewhat complicated. To enable an appreciation of the processes at play, we have supposed that the imposed surface vibration takes the form of a single Fourier mode. In a practical setting, it would be expected that any boundary perturbation would consist of several components of various wavelengths. One could derive the associated stability properties only by conducting careful calculations replicating the exact vibration profile; this may prove difficult. On the other hand, an investigation into the spectrum of vibrations should facilitate the identification of any waves present that might prove particularly effective in causing instability. Such considerations would also provide a means for selecting possible structures for those vibrations that might prove good candidates for achieving some specified control flow objective; conceivably, this might be to reduce the flow resistance, provide a propulsion effect, or increase the efficacious of fluid mixing. Streamwise vortices are particularly relevant to mixing intensification as they include a component of the transverse transport of scalar quantities.

In summary, the considerations described above constitute some of the first calculations aimed at throwing light on the properties of simple shear flows when modified by surface vibrations. We have seen that the situation is somewhat intricate, and there is much scope for extension into various regimes, such as large-amplitude vibrations and practically-important shear flows. We hope to explore and report on some of these avenues in due course.

Declaration of interests. The authors report no conflict of interest.

Appendix A

We find a form of the pressure gradient constraint suitable for numerical implementation.
Start with the explicit form of (3.7), i.e.

$$\psi_{1,B}(x, \hat{y}) = \sum_{n=-N_B}^{+N_B} \psi_{1,B}^{(n)}(\hat{y}) e^{in\alpha x}, \quad u_{1,B}(x, \hat{y}) = \sum_{n=-N_B}^{+N_B} u_{1,B}^{(n)}(\hat{y}) e^{in\alpha x},$$

$$(A1a,b)$$

$$v_{1,B}(x, \hat{y}) = \sum_{n=-N_B}^{+N_B} v_{1,B}^{(n)}(\hat{y}) e^{in\alpha x}, \quad \widehat{u_{1,B} u_{1,B}}(x, \hat{y}) = \sum_{n=-N_B}^{+N_B} \widehat{u_{1,B} u_{1,B}}^{(n)}(\hat{y}) e^{in\alpha x},$$

$$(A1c,d)$$

$$\widehat{u_{1,B}v_{1,B}}(x, \hat{y}) = \sum_{n=-N_B}^{+N_B} \widehat{u_{1,B}v_{1,B}}^{(n)}(\hat{y})e^{in\alpha x}, \quad \widehat{v_{1,B}v_{1,B}}(x, \hat{y}) = \sum_{n=-N_B}^{+N_B} \widehat{v_{1,B}v_{1,B}}^{(n)}(\hat{y})\, e^{in\alpha x},$$

$$\text{(A1}e,f)$$

$$p_{1,B}(x, \hat{y}) = -Bx + \sum_{n=-N_B}^{+N_B} p_{1,B}^{(n)}(\hat{y})\, e^{in\alpha x}, \tag{A1g}$$

where B is the linear pressure gradient correction. Use of the definition of the stream function, i.e.

$$u_{1,B} = \frac{\partial \psi_{1,B}}{\partial y} = \Gamma \frac{\partial \psi_{1,B}}{\partial \hat{y}}, \quad v_{1,B} = -\frac{\partial \psi_{1,B}}{\partial x}, \tag{A2a,b}$$

leads to

$$u_{1,B} = \Gamma \sum_{n=-N_B}^{+N_B} D\psi_{1,B}^{(n)}(\hat{y})e^{in\alpha x}, \quad v_{1,B} = -i\alpha \sum_{n=-N_B}^{+N_B} n\psi_{1,B}^{(n)}(\hat{y})\, e^{in\alpha x}. \tag{A3}$$

The x-momentum equation written in terms of the reference flow and flow modifications has the form

$$\frac{\partial p_{1,B}}{\partial x} = -(Re\, u_0 - c)\frac{\partial u_{1,B}}{\partial x} - Re\frac{du_o}{dy}v_{1,B} + \frac{\partial^2 u_{1,B}}{\partial x^2} + \frac{\partial^2 u_{1,B}}{\partial y^2} - u_{1,B}\frac{\partial u_{1,B}}{\partial x}$$

$$- v_{1,B}\frac{\partial u_{1,B}}{\partial y}. \tag{A4}$$

Writing (A4) in the $(x, \hat{y})$-coordinates in terms of the stream function yields

$$\frac{\partial p_{1,B}}{\partial x} = -(Re\, u_0 - c)\frac{\partial}{\partial x}\left(\Gamma\frac{\partial \psi_{1,B}}{\partial \hat{y}}\right) - Re\frac{du_o}{dy}\left(-\frac{\partial \psi_{1,B}}{\partial x}\right) + \frac{\partial^2}{\partial x^2}\left(\Gamma\frac{\partial \psi_{1,B}}{\partial \hat{y}}\right)$$

$$+ \Gamma^2\frac{\partial^2}{\partial \hat{y}^2}\left(\Gamma\frac{\partial \psi_{1,B}}{\partial \hat{y}}\right) - \frac{\partial}{\partial x}(u_{1,B}u_{1,B}) - \Gamma\frac{\partial}{\partial \hat{y}}(u_{1,B}v_{1,B}). \tag{A5}$$

Substitution of (A1) into (A5) and separation of Fourier modes results in modal equations of the form

$$-B + in\alpha p_{1,B}^{(n)} = -(Re\, u_0 - c)\,\Gamma in\alpha D\psi_{1,B}^{(n)} + Re\frac{du_o}{dy}in\alpha\psi_{1,B}^{(n)}$$

$$- \Gamma n^2\alpha^2 D\psi_{1,B}^{(n)} + \Gamma^3 D^3\psi_{1,B}^{(n)} - in\alpha\widehat{u_{1,B}u_{1,B}}^{(n)}$$

$$- \Gamma D\widehat{u_{1,B}v_{1,B}}^{(n)}. \tag{A6}$$

The above equation reduced for mode zero has the form

$$B = -\Gamma^3 D^3\psi_{1,B}^{(0)} + \Gamma D\widehat{u_{1,B}v_{1,B}}^{(0)}. \tag{A7}$$

Integration of (A7) between $+1$ and -1 leads to

$$2B = -\Gamma^3\left[D^2\psi_{1,B}^{(0)}(+1) - D^2\psi_{1,B}^{(0)}(-1)\right]$$

$$+ \Gamma\left[\widehat{u_{1,B}v_{1,B}}^{(0)}(+1) - \widehat{u_{1,B}v_{1,B}}^{(0)}(-1)\right]. \tag{A8}$$

The fixed pressure gradient constraint requires that $B = 0$, which reduces (A8) to

$$D^2\psi_{1,B}{}^{(0)}(+1) - D^2\psi_{1,B}{}^{(0)}(-1) = \Gamma^{-2}[\widehat{u_{1,B}v_{1,B}}{}^{(0)}(+1) - \widehat{u_{1,B}v_{1,B}}{}^{(0)}(-1)], \quad \text{(A9)}$$

which is the form of the pressure gradient constraint suitable for numerical implementation.

Appendix B

Definitions of operators used in (4.7):

$$D^q = \frac{\mathrm{d}^q}{\mathrm{d}y^q}, \quad t_m = \delta + m\alpha, \quad k_m^2 = t_m^2 + \mu^2, \quad \text{(B1)}$$

$$T^{<m>} = \left(D^2 - k_m^2\right)^2 + i\sigma\left(D^2 - k_m^2\right) + ict_m\left(D^2 - k_m^2\right),$$

$$S^{<m>} = \left(D^2 - k_m^2\right) + i\sigma + ict_m, \quad \text{(B2)}$$

$$T_1^{<m-n>} = \frac{it_{m-n}}{k_{m-n}^2}\left(-t_m^2 Df_u^{<n>}D + in\alpha k_m^2 f_v^{<n>}D - t_m^2 f_u^{<n>}D^2 + it_m Df_v^{<n>}D^2\right.$$
$$\left. + it_m f_v^{<n>}D^3\right), \quad \text{(B3)}$$

$$T_2^{<m-n>} = ik_m^2 t_{m-n} f_u^{<n>} + k_m^2 Df_v^{<n>} + k_m^2 f_v^{<n>}D + it_m D^2 f_u^{<n>} + it_m Df_u^{<n>}D, \quad \text{(B4)}$$

$$T_3^{<m-n>} = \frac{i\mu}{k_{m-n}^2}\left(-\mu t_{m-2n} f_u^{<n>}D^2 + i\mu f_v^{<n>}D^3 - \mu t_{m-n} Df_u^{<n>}D\right), \quad \text{(B5)}$$

$$T_4^{<m-n>} = \frac{it_{m-n}}{k_{m-n}^2}\left(-\mu t_{m-2n} f_u^{<n>}D + i\mu f_v^{<n>}D^2 - \mu t_{m-n} Df_u^{<n>}\right), \quad \text{(B6)}$$

$$T_5^{<m-n>} = \frac{i\mu}{k_{m-n}^2}\left(-t_m^2 Df_u^{<n>} + in\alpha k_m^2 f_v^{<n>} - t_m^2 f_u^{<n>}D + it_m Df_v^{<n>}D\right.$$
$$\left. + it_m f_v^{<n>}D^2\right), \quad \text{(B7)}$$

$$S_1^{<m-n>} = \frac{i\mu}{k_{m-n}^2}\left(t_{m-n}t_m f_u^{<n>}D - it_m f_v^{<n>}D^2\right), \quad \text{(B8a)}$$

$$S_2^{<m-n>} = i\mu Df_u^{<n>}, \quad \text{(B8b)}$$

$$S_3^{<m-n>} = \frac{it_{m-n}}{k_{m-n}^2}\left(i\mu f_v^{<n>}D^2 - \mu t_m f_u^{<n>}D\right), \quad \text{(B8c)}$$

$$S_4^{<m-n>} = \frac{it_{m-n}}{k_{m-n}^2}\left(t_{m-n}t_m f_u^{<n>} - it_m f_v^{<n>}D\right), \quad \text{(B8d)}$$

$$S_5^{<m-n>} = \frac{i\mu}{k_{m-n}^2}\left(i\mu f_v^{<n>}D - \mu t_m f_u^{<n>}\right). \quad \text{(B8e)}$$

REFERENCES

ABTAHI, A. & FLORYAN, J.M. 2017 Natural convection and thermal drift. *J. Fluid Mech.* **826**, 553–582.

BEWLEY, R. 2009 A fundamental limit on the balance of power in a transpiration-controlled channel flow. *J. Fluid Mech.* **632**, 443–446.

BLAKE, J.R. & SLEIGH, M.A. 1974 Mechanics of ciliary locomotion. *Biol. Rev.* **49** (1), 85–125.

BRENNEN, C. & WINET, H. 1977 Fluid mechanics of propulsion by cilia and flagella. *Ann. Rev. Fluid Mech.* **9** (1), 339–398.

CANUTO, C., HUSSAINI, M.Y., QUARTERONI, A. & ZANG, T.A. 1992 *Spectral Methods in Fluid Dynamics*. Springer.

CHAN, B., BALMFORTH, N.J. & HOSOI, A.E. 2005 Lubrication and adhesive locomotion. *Phys. Fluids* **19**, 113101.

FLORYAN, D. 2023 A fundamental limit on energy savings in controlled channel flow, and how to beat it. *J. Fluid Mech.* **954**, R3.

FLORYAN, D. & FLORYAN, J.M. 2015 Drag reduction in heated channels. *J. Fluid Mech.* **765**, 353–395.

FLORYAN, J.M. 1991 On the Görtler instability of boundary layers. *Prog. Aerospace Sci.* **28** (3), 235–271.

FLORYAN, J.M. 1997 Stability of wall bounded shear layers with simulated distributed surface roughness. *J. Fluid Mech.* **335**, 29–55.

FLORYAN, J.M. 2002 Centrifugal instability of Couette flow over a wavy wall. *Phys. Fluids* **14** (1), 312–322.

FLORYAN, J.M. 2007 Three-dimensional instabilities of laminar flow in a rough channel and the concept of a hydraulically smooth wall. *Eur. J. Mech. B/Fluids* **26** (3), 305–329.

FLORYAN, J.M., AMAN, S.A. & PANDAY, S. 2023 Propulsion due to thermal streaming. *J. Fluid Mech.* **967**, A13.

FLORYAN, J.M. & HAQ, H. 2022 The role of vibrations for reduction of resistance in relative movement of parallel plates. *J. Fluid Mech.* **949**, A28.

FLORYAN, J.M. & INASAWA, A. 2021 Pattern interaction effect. *Sci. Rep.* **11** (1), 14573.

GEPNER, S.W. & FLORYAN, J.M. 2020 Use of surface corrugations for energy-efficient chaotic stirring in low Reynolds number flows. *Sci. Rep.* **10** (1), 1–8.

HAQ, N.N. & FLORYAN, J.M. 2022 Propulsive effect of wall vibrations. *ASME J. Fluids Eng.* **144**, 121204.

HOSSAIN, M. & FLORYAN, J.M. 2023 Pumping using thermal waves. *J. Fluid Mech.* **966**, A43.

HUSAIN, S.Z., SZUMBARSKI, J. & FLORYAN, J.M. 2009 Over-constrained formulation of the immersed boundary condition method. *Comp. Meth. Appl. Mech. Engng* **199** (1–4), 94–112.

JIAO, L. & FLORYAN, J.M. 2021 On the use of transpiration for reduction of resistance to relative movement of parallel plates. *Phys. Rev. Fluids* **6** (1), 014101.

KATZ, D.F. 1974 On the propulsion of micro-organisms near solid boundaries. *J. Fluid Mech.* **64** (1), 33–49.

LAUGA, E. 2016 Bacterial hydrodynamics. *Ann. Rev. Fluid Mech.* **48** (1), 105–135.

LEE, S., BUSH, J.W.M., HOSOI, A.E. & LAUGA, E. 2008 Crawling beneath the free surface: water snail locomotion. *Phys. Fluids* **20** (8), 082106.

LEIBOVICH, S. 1983 The form and dynamics of Langmuir circulations. *Ann. Rev. Fluid Mech.* **15** (1), 391–427.

PANDAY, S. & FLORYAN, J.M. 2023 Accurate determination of stability characteristics of spatially modulated shear layers. *J. Fluid Mech.* **975**, A50.

PARK, J., HWANG, H. & COSSU, C. 2011 On the stability of large-scale streaks in turbulent Couette and Poiseuille flows. *Comptes Rendus Mécanique* **339**, 1–5.

ROMANOV, V.A. 1972 Stability of plane-parallel Couette flow. *Funct. Anal. Applics* **7**, 137–146.

SCHMID, P.S. & HENNINGSON, D.S. 2001 *Stability and Transition in Shear Flows, Applied Mathematical Sciences 142*. Springer.

SZUMBARSKI, J. & FLORYAN, J.M. 1999 A direct spectral method for determination of flows over corrugated boundaries. *J. Comp. Phys.* **153** (2), 78–402.

TAYLOR, G. 1951 Analysis of the swimming of microscopic organisms. *Proc. R. Soc. Lond. A* **209** (1099), 447–461.

THORPE, S.A. 2004 Langmuir circulation. *Ann. Rev. Fluid Mech.* **36** (1), 55–79.

TILLMARK, N. & ALFREDSSON, P. 1992 Experiments on transition in plane Couette flow. *J. Fluid Mech.* **235**, 89–102.